nature materials

ARTICLES

https://doi.org/10.1038/s41563-018-0204-4

Ferroelectrically tunable magnetic skyrmions in ultrathin oxide heterostructures

Lingfei Wang[1,2*], Qiyuan Feng[3,4,8], Yoonkoo Kim[5,8], Rokyeon Kim[1,2,8], Ki Hoon Lee[1,2,8], Shawn D. Pollard[6], Yeong Jae Shin[1,2], Haibiao Zhou[1,2,3], Wei Peng[1,2], Daesu Lee[1,2], Wenjie Meng[3], Hyunsoo Yang[6], Jung Hoon Han[7], Miyoung Kim[5], Qingyou Lu[3,4*] and Tae Won Noh[1,2*]

Magnetic skyrmions are topologically protected whirling spin texture. Their nanoscale dimensions, topologically protected stability and solitonic nature, together are promising for future spintronics applications. To translate these compelling features into practical spintronic devices, a key challenge lies in achieving effective control of skyrmion properties, such as size, density and thermodynamic stability. Here, we report the discovery of ferroelectrically tunable skyrmions in ultrathin $BaTiO_3$/$SrRuO_3$ bilayer heterostructures. The ferroelectric proximity effect at the $BaTiO_3$/$SrRuO_3$ heterointerface triggers a sizeable Dzyaloshinskii–Moriya interaction, thus stabilizing robust skyrmions with diameters less than a hundred nanometres. Moreover, by manipulating the ferroelectric polarization of the $BaTiO_3$ layer, we achieve local, switchable and nonvolatile control of both skyrmion density and thermodynamic stability. This ferroelectrically tunable skyrmion system can simultaneously enhance the integratability and addressability of skyrmion-based functional devices.

Magnetic skyrmions are nanoscale swirling spin texture exhibiting nontrivial real-space topology[1,2]. Since the first observation in 2009[3], this chiral spin configuration has been investigated intensively due to a variety of exotic characteristics, including topological protection from defects and disorder[4,5]; compact and self-organized lattice forms[3,6–8]; and a solitonic nature allowing excitation, annihilation and controlled motion[4,9–13]. These compelling features offer not only new opportunities for investigating non-trivial topological physics but also great potential for future spintronics applications[2,13]. In view of realizing skyrmion-based spintronic devices with high integration levels and superior performance, it is essential to achieve effective control of skyrmion properties, including size, density and stability[2].

Magnetic skyrmions are, in most cases, driven by the Dzyaloshinskii–Moriya interaction (DMI)[14–16]. This chiral interaction stems from both spin–orbit coupling (SOC) and inversion-symmetry-breaking[13,15]. Unlike the exchange interaction, which always aligns spins, the DMI tends to whirl spins, which makes it the key to manipulating skyrmion properties[17]. Specifically, the stability of magnetic skyrmions can be evaluated by the critical DMI constant $D_C = 4\sqrt{JK}/\pi$, where J and K are the exchange stiffness and out-of-plane magnetic anisotropy, respectively[2]. For non-centrosymmetric ferromagnets, such as the B20 compounds, Cu_2OSeO_3 and GaV_4S_8, the relatively larger DMI constant (D) over D_C can stabilize skyrmions in a compact lattice form with typical diameters in the approximate range from 10 to 100 nm (refs [6–8,18,19]). However, the magnetic interactions for specific bulk compounds are almost invariant. In contrast, skyrmions in heavy-metal/ferromagnet multilayers are highly sensitive to the stacking sequences, layer compounds, and various external stimuli[20–25]. A locally imposed spin-transfer torque, electric field, or current gradient can trigger in-situ control of skyrmion properties and even nucleation/annihilation of individual skyrmions[4,9–13,22–25]. Nevertheless, the smaller D compared to D_C commonly leads to metastable and isolated skyrmions, and the typical skyrmion diameter is in the range from several hundred nanometres to micrometres[9–11,22,23], which could hinder the degree of integration in practical devices[2]. Although numerous skyrmion systems have been discovered, the contradiction between miniaturization and controllability has not been fully resolved[12,25].

Ferroelectricity is one of the best-studied long-range ferroic orders with inversion-symmetry-breaking[26]. The nonvolatile, switchable nature of ferroelectric (FE) polarization renders the degree and direction of inversion-symmetry-breaking eminently tunable. Thus, integrating ferroelectricity into magnetic skyrmion systems, if realized, would offer a great potential to enhance the electrical controllability. This paradigm has been corroborated by recent reports on the multiferroic compound GaV_4S_8, in which magnetic skyrmions and spontaneous electric polarization coexist and strongly couple with each other[27]. Very recently, possible magnetic skyrmion states were also proposed and observed in a variety of epitaxial oxide heterostructures[24,28–30]. These epitaxial systems further imply greater flexibility and the possibility of coupling ferroelectricity and magnetic skyrmions via artificially designed heterointerfaces[31].

In the present work, we report the discovery of FE-driven, highly tunable magnetic skyrmions in ultrathin $BaTiO_3$/$SrRuO_3$ (BTO/SRO) bilayer heterostructures. As schematically shown in Fig. 1a, FE-driven ionic displacements in BTO may cross the heterointerface

[1]Center for Correlated Electron Systems, Institute for Basic Science (IBS), Seoul, Republic of Korea. [2]Department of Physics and Astronomy, Seoul National University, Seoul, Republic of Korea. [3]Anhui Province Key Laboratory of Condensed Matter Physics at Extreme Conditions, High Magnetic Field Laboratory, Chinese Academy of Sciences, Hefei, Anhui, China. [4]Hefei National Laboratory for Physical Sciences at the Microscale, University of Science and Technology of China, Hefei, Anhui, China. [5]Department of Materials Science and Engineering and Research Institute of Advanced Materials, Seoul National University, Seoul, Republic of Korea. [6]Department of Electrical and Computer Engineering, National University of Singapore, Singapore, Singapore. [7]Department of Physics, Sungkyunkwan University, Suwon, Republic of Korea. [8]These authors contributed equally: Qiyuan Feng, Yoonkoo Kim, Rokyeon Kim and Ki Hoon Lee. *e-mail: lingfei.wang@outlook.com; qxl@ustc.edu.cn; twnoh@snu.ac.kr

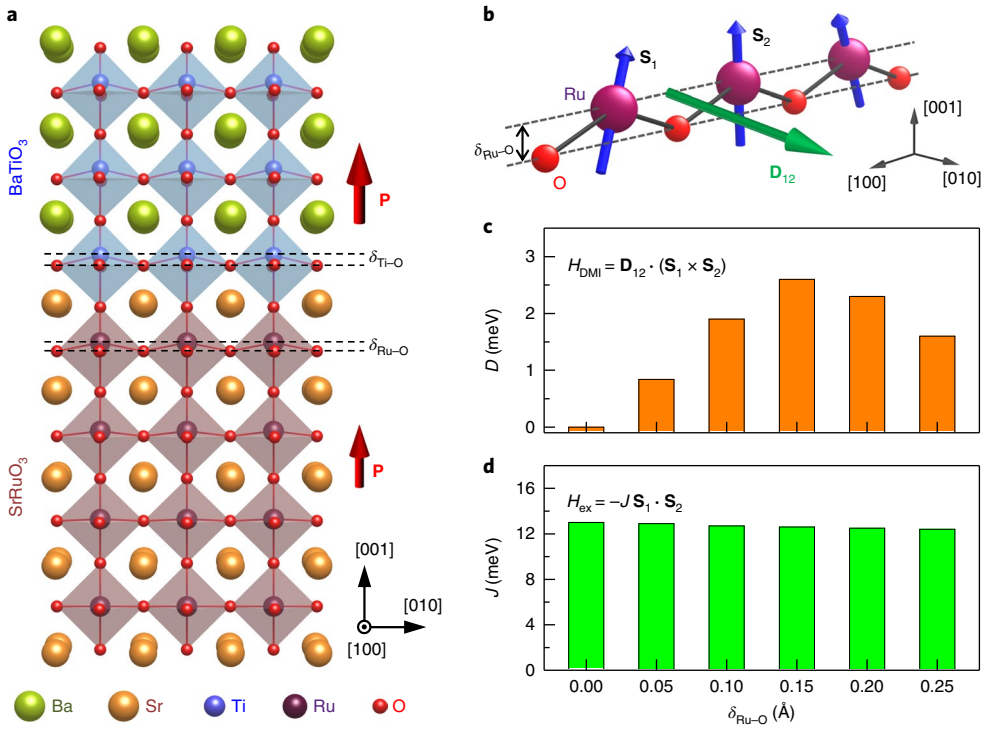

Fig. 1 | Ferroelectric proximity effect and the DMI at the BTO/SRO interface. a, Schematic diagram of the ferroelectric (FE) proximity effect at the BTO/SRO interface. FE-driven ionic displacement in BTO can penetrate into SRO to a depth of several unit cells (u.c.). The ionic displacement between oxygen and Ti (Ru) along the [001] axis is denoted as $\delta_{\text{Ti-O}}$ ($\delta_{\text{Ru-O}}$). **b**, A sketch of the DMI in SRO with non-zero $\delta_{\text{Ru-O}}$. The DMI vector $\mathbf{D}_{12}$ is perpendicular to the imaginary triangle defined by the two Ru cations and an oxygen ligand in between. **c**,**d**, Density functional theory (DFT) calculation results of the DMI constant (D) (**c**) and exchange stiffness (J) (**d**).

and continue for several unit cells into SRO. This so-called FE proximity effect has been both predicted and demonstrated in various FE/metallic oxide heterointerfaces[32–35]. In our BTO/SRO heterostructures, this effect can induce a sizeable DMI, thus stabilizing robust magnetic skyrmions. Furthermore, by harnessing the FE polarization of the BTO capping layer, we can achieve local, reversible and nonvolatile control of skyrmion properties. This ferroelectrically tunable skyrmion system suggests a potential direction for designing skyrmion-based functional devices with high integration levels and addressability.

Emergent DMI at the BTO/SRO interface

We first explore the microscopic origin of the DMI at the BTO/SRO heterointerface. SRO, a 4*d* transition-metal-oxide, has an SOC strength of 0.1~0.15 eV (ref. [36]). The lattice distortion driven by the FE proximity effect breaks the inversion symmetry of the SRO structure near the BTO/SRO interface. Considering a [001]-oriented FE polarization (Fig.1a), the degree of inversion-symmetry-breaking in SRO can be described as the vertical ionic displacement between Ru and O in the RuO_2 plane ($\delta_{\text{Ru-O}}$)[32–35,37]. By taking the analogy to multiferroics consisting of spiral magnetic ordering[26], we expect an emergent DMI in the ferroelectrically distorted SRO lattice. Given two neighbouring spins $\mathbf{S}_1$ and $\mathbf{S}_2$ in SRO, the Hamiltonian of the DMI is defined as follows:

$H_{\text{DMI}} = \mathbf{D}_{12} \cdot (\mathbf{S}_1 \times \mathbf{S}_2)$, where the DMI vector is given by $\mathbf{D}_{12} = D\hat{\mathbf{r}}_{12} \times \hat{\mathbf{z}}$. Here $\hat{\mathbf{z}}$ and $\hat{\mathbf{r}}_{12}$ represent unit vectors along the [001] axis and pointing from $\mathbf{S}_1$ to $\mathbf{S}_2$, respectively. As schematically depicted in Fig. 1b, $\mathbf{D}_{12}$ should lie in-plane, perpendicular to the Ru–O–Ru chains[15,16].

To validate this plausible mechanism of ferroelectrically-driven DMI, we performed ab initio density functional theory (DFT) calculations on the magnetic interactions in SRO with various $\delta_{\text{Ru-O}}$ (see Methods and Supplementary Section 1 for details). As shown in Fig. 1c, the calculated D first increases almost linearly with $\delta_{\text{Ru-O}}$, similar to the trend noted in spiral-ordered multiferroics[26]. Further increasing $\delta_{\text{Ru-O}}$ above 0.2 Å leads to a slight reduction in D, possibly due to changes in electronic structure. In contrast, the calculated J (Fig. 1d) remains nearly unchanged as $\delta_{\text{Ru-O}}$ increases. At $\delta_{\text{Ru-O}} = 0.15$ Å, D and D/J attain maxima of 2.30 meV and 0.18, respectively. Both parameters are comparable to the typical values in previously reported skyrmion systems[20,21]. Accordingly, we expected that this in-plane DMI near the BTO/SRO interface may stabilize Néel-type magnetic skyrmions[13].

Topological Hall effect in BTO/SRO heterostructures

The BTO/SRO heterostructures were epitaxially grown on atomically-flat $SrTiO_3$(001) [STO(001)] substrates using pulsed laser deposition (see Methods and Supplementary Section 2 for details)[38]. The thicknesses of SRO (t_{SRO}) and BTO (t_{BTO}) were precisely controlled on a unit-cell scale. The epitaxial quality, ferroelectricity, electrical transport and magnetism of the BTO/SRO heterostructures have been comprehensively characterized (Supplementary Sections 2–4). These basic physical properties are consistent with those in previously reported BTO and SRO ultrathin films[30,38,39].

We first explored possible magnetic skyrmions in the BTO/SRO heterostructures via Hall measurements. In a prototypical magnetic skyrmion system, the transverse Hall resistivity ρ_{xy} can be decomposed into $\rho_{xy} = \rho_{\text{OHE}} + \rho_{\text{AHE}} + \rho_{\text{THE}}$, where the three terms denote the ordinary, anomalous and topological Hall resistivities, respectively[1]. The ordinary Hall effect (OHE) is described by $\rho_{\text{OHE}} = R_0 H$, where R_0 and H are the ordinary Hall coefficient and out-of-plane magnetic field, respectively. For all of the Hall results shown below, the OHE contribution has been subtracted by fitting the linear slope of the ρ_{xy}–H curve at $\mu_0 H \geq 5$ T. The anomalous Hall effect (AHE) is

generally expressed as $\rho_{AHE} = R_s M$, where R_s and M are cumulative AHE coefficient and magnetization, respectively[39]. The topological Hall effect (THE) arises from the Berry phase acquired by conduction electrons as they pass through a skyrmion[1,23]. In the limit of strong exchange coupling between the electron spin and local M in the skyrmion, the THE contribution is expressed as follows

$$\rho_{THE} = P_s R_0 n_{sk} h/e \quad (1)$$

where P_s, n_{sk}, h and e denote the spin polarization of carriers, skyrmion density, Planck constant and elementary charge, respectively. For SRO, we estimate $P_s = -10 \pm 5\%$ (refs [30,39]).

The Hall signals of SRO/BTO samples are strongly dependent on the bilayer structure (that is, t_{SRO} and t_{BTO}). As shown in Fig. 2a, the ρ_{xy}–H curve of the BTO(20 u.c.)/SRO(8 u.c.) sample (B20S8) at 10 K (where u.c. is unit cell) is similar to an inverted ferromagnetic M–H loop, signifying a dominant AHE with negative R_s. As t_{SRO} decreases to 5 u.c. (B20S5), the ρ_{xy}–H curve clearly shows two additional non-monotonic humps at ±2.5 T, which cannot be assigned to the AHE. Recently, similar ρ_{xy}–H behaviour was reported in $SrIrO_3$/SRO bilayer skyrmion systems[24,30]. On this basis, we suggest that these humps should be assigned to the THE with a skyrmionic nature. As t_{SRO} decreases to 4 u.c. (B20S4), the AHE hysteresis loop becomes slimmer and the THE humps become prominent, indicating the appearance of high-density skyrmions. In addition, as t_{BTO} decreases from 8 u.c. to 0 (Fig. 2b), the THE feature becomes gradually suppressed and finally vanishes.

We further investigated the basic skyrmion properties by precisely determining ρ_{THE}. Taking the B20S4 sample as an example (Fig. 2c), we measured the M–H curve and used it to fit the ρ_{AHE} contribution[21,30]. By subtracting ρ_{OHE} and ρ_{AHE} from ρ_{xy}, we obtained the ρ_{THE}–H curve. When H is aligned parallel with the core spin orientation of the skyrmion and approaches the coercive field (H_C), ρ_{THE} increases sharply and peaks at approximately ±1.65 T. Further sweeping H across H_C, ρ_{THE} starts to decrease gradually and vanishes at the critical field $\mu_0 H_{sk} = \pm 3.9$ T, at which the M–H hysteresis loop closes also. The ρ_{THE}–H behaviour strongly indicates that the skyrmions are excitations from the ferromagnetic background, and their emergence is assisted by the ferromagnetic domain switching. This behaviour, distinct from conventional skyrmion systems with a helix ground state[6,21], can be further corroborated by the micromagnetic simulations (Supplementary Section 5). According to the ρ_{THE}–H curves measured at various temperatures (Supplementary Section 4), the THE of the B20S4 sample can persist up to 80 K (close to the Curie temperature of approximately 100 K) and even at zero field, which highlights the robustness of these FE-driven skyrmions.

The evolution of n_{sk} (estimated from ρ_{THE} and equation (1)) with sample structures (here, t_{SRO} and t_{BTO}) provides important information about the origin of skyrmions. On one hand, the fast decay of n_{sk} as t_{SRO} increases (Fig. 2d) implies that the driving force of skyrmions should be located close to the heterointerface. On the other hand, as t_{BTO} decreases below 8 u.c., n_{sk} reduces dramatically (Fig. 2e) in association with the suppression of the FE polarization. This trend further demonstrates that skyrmions should be FE-driven, probably through the FE proximity effect.

Magnetic force microscopy of BTO/SRO heterostructure

Real-space imaging of the microscopic magnetic texture is highly desired to further support the existence of skyrmions. Accordingly, we performed magnetic force microscopy (MFM) measurements on the B20S5 sample (see Methods), in which both M and ρ_{THE} have moderate magnitudes (Fig. 3j). MFM images were obtained at various values of H ranging from 5 to −5 T. Representative images and the full set of images are shown in Fig. 3a–e and Supplementary Section 6, respectively. Figure 3a, taken at the fully saturated ferromagnetic state, exhibits a weak and stripe-like MFM contrast, which can be explained by the local inhomogeneities in both t_{SRO} and magnetism near the terrace edges[39]. This poor MFM contrast, together with the weak overall magnetism and small skyrmion size, makes direct imaging of skyrmions challenging. To improve the imaging quality, we applied a pixel-by-pixel subtraction operation to every two adjacent images measured from −2.5 to −2.9 T. Because of the minor variation of M in this H range, the invariant MFM contrast from terrace edges cancels out after the subtraction operation. As shown in Fig. 3f,g, the processed MFM images clearly exhibit numerous magnetic domain-like contrasts (blue) against a uniform background (yellow). These MFM signals should be related to either magnetic skyrmions or magnetic bubble domains that emerge as H changes.

We can classify the MFM contrasts into two categories (Type 1 and 2) according to their shapes and sizes. Type 1 MFM contrasts, appearing in all of the subtracted images, have rather uniform sizes and circular shapes. In the histogram of equivalent diameters (Fig. 3h), these MFM contrasts correspond to the narrow Gaussian distribution peaked at ~90 nm. Their uniformity in size and magnitude can be further corroborated by the similar MFM line profiles shown in Fig. 3i. These results strongly suggest that the Type 1 MFM contrasts probably originate from individual skyrmions. Compared with magnetic bubble domains, skyrmions tend to have much more uniform size and circular shapes in the small H range (−2.5 to −2.9 T). Type 2 MFM contrasts have larger sizes and irregular shapes, corresponding to the much broader Gaussian distribution peaked at ~160 nm. According to the observed large diversities in morphology, Type 2 MFM contrasts should be assigned to either magnetic bubble domains or skyrmion clusters. The magnetic bubble domains could be topologically equivalent to one or multiple skyrmions, and the skyrmion clusters are formed by multiple adjacent skyrmions[40]. Due to the inadequate spatial resolution of MFM, the true spin texture of the Type 2 contrasts remains an open question. It could be investigated further using other real-space imaging techniques with higher resolution—for example, Lorentz transmission electron microscopy[40,41].

MFM results can provide important information about skyrmion size and density. As shown in Fig. 3i, the full-width-at-half-maximum (FWHM) of the Type 1 MFM profile is ~90 nm, which could be much wider than the real skyrmion diameter due to broadening from the MFM tip and skyrmion stray field[21,42]. By taking this factor into account, we estimated that the size of individual skyrmions could be in the range 50–100 nm (see procedural details in Supplementary Section 6). We further calculated the changes in n_{sk} (Δn_{sk}) as H increases from −2.5 T to −2.9 T. As shown in Fig. 3k, Δn_{sk} derived from MFM images and those calculated from equation (1) share the same trend, which confirms the strong correlation between the THE and n_{sk}. However, quantitatively, Δn_{sk} derived from MFM images are consistently a factor of five less than the values calculated from equation (1). This discrepancy can be explained by the relatively weak exchange coupling in BTO/SRO samples and resultant non-adiabatic contribution of ρ_{THE} (Supplementary Section 7)[43]. Notably, the proportional relationship between ρ_{THE} and n_{sk} prevails in both strong and weak exchange coupling cases. Hence, we can still use ρ_{THE} as a reliable probe to investigate the skyrmion properties.

Ferroelectric control of skyrmion properties

Next, we demonstrated the prominent tunability of FE-driven skyrmions in BTO/SRO heterostructures. Because of the strongly correlated DMI and ferroelectricity, we may be able to tune the skyrmion properties simply by switching the FE polarization. Here, we employed an atomic force microscopy (AFM)-based electric gating approach to realize the FE-mediated controllability (see Methods and Supplementary Section 8 for details)[44,45]. As depicted in Fig. 4a, we first selectively poled certain areas of the B20S4 sample Hall bar at room temperature using a biased conducting AFM tip (tip bias

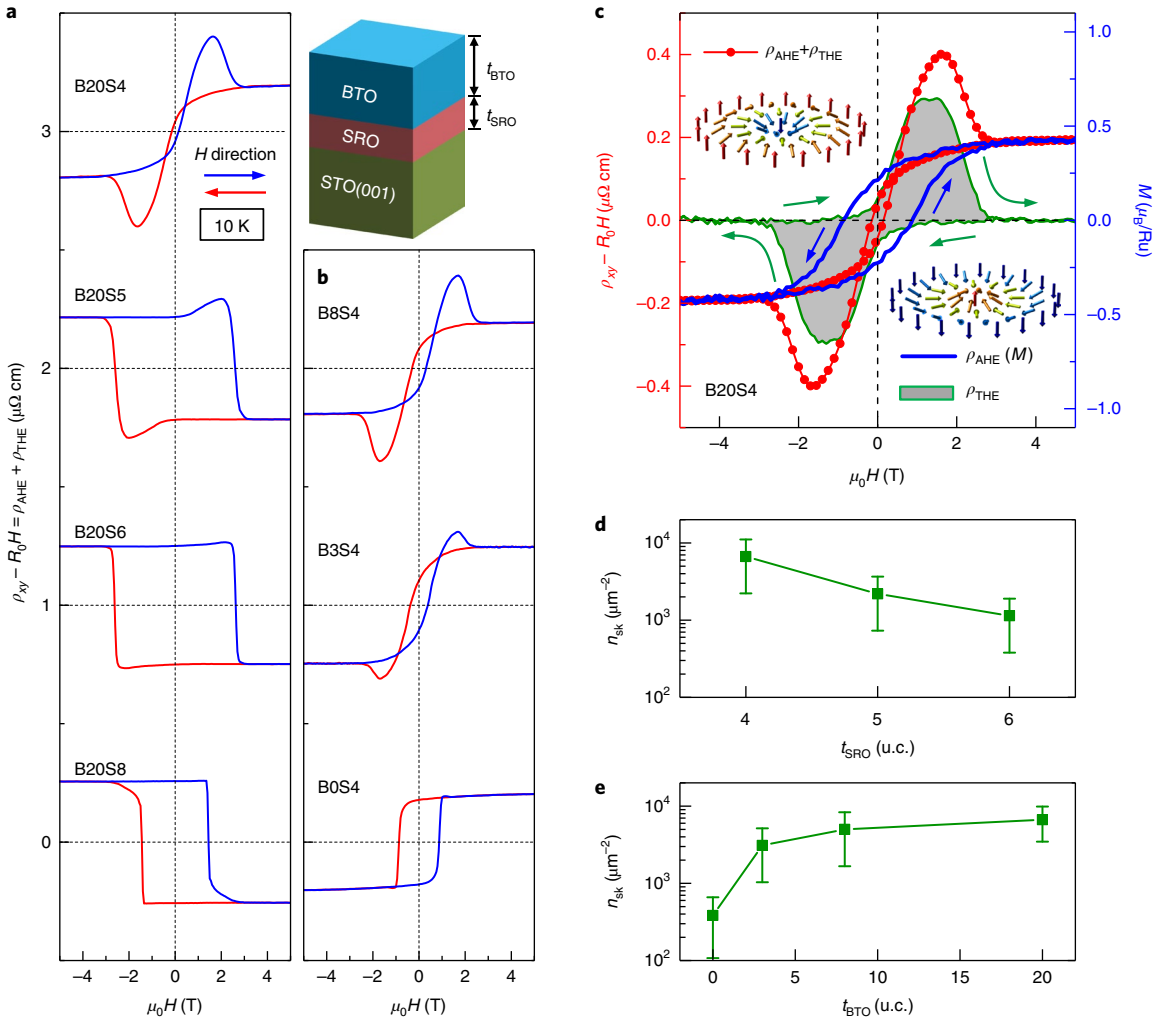

Fig. 2 | Topological Hall effects of BTO/SRO/SrTiO$_3$(001) heterostructures. a,**b**, Magnetic-field-dependent Hall resistivity (ρ_{xy}-H) curves at 10 K obtained from BTO/SRO samples with various SRO layer thickness (t_{SRO}) (**a**) and BTO layer thickness (t_{BTO}) (**b**). The BTO(20 u.c.)/SRO(4 u.c.) sample is denoted as B20S4, and the same notation applies for other BTO/SRO samples. The red and blue colours represent the H-sweeping directions. The linear contribution from the OHE has been subtracted from all curves. The inset is the schematic sample structure. **c**, ρ_{xy}, ρ_{AHE} and ρ_{THE} versus H for the B20S4 sample. The ρ_{AHE}-H curve is derived from the normalized M-H curve. The unit of M is Bohr magneton per Ru atom (μ_B/Ru). The H-sweeping directions are marked by solid arrows. **d**,**e**, Skyrmion density (n_{sk}) versus t_{SRO} and t_{BTO} calculated from equation (1). The error bars are given by the uncertainty of the carrier spin polarization $P_S = -10 \pm 5$ %.

$V_{tip} = \pm 8$ V). Then we cooled the sample below 100 K and investigated the skyrmion properties by measuring ρ_{THE}. It is noteworthy that the pre-poled FE domain patterns remain stable throughout the Hall measurements (Supplementary Section 3), which manifests the nonvolatile nature of this FE-mediated controllability.

Local switching of the BTO polarization leads to marked changes in the THE. As shown in Fig. 4b, we first poled the entire conducting channel with $V_{tip} = -8$ V, achieving upward polarization in BTO. After cooling to 10 K, the uniformly upward-poled Hall bar exhibits a slight enhancement in ρ_{THE} compared with that in the pristine FE state (multi-domain structure with a preferential upward polarization, shown in Supplementary Section 3). We then divided the channel into three stripes and sequentially reversed the FE polarization of these regions with $V_{tip} = +8$ V. The selectively poled stripe regions clearly exhibit stable and uniformly downward polarization, as shown in the top panels of Fig. 4c–e. After sequentially poling the polarization of the stripe regions to downward, ρ_{THE} (bottom panels in Fig. 4c,d) decreases gradually. For the full downward-poling case (Fig. 4e), ρ_{THE} decreases by ~80%, signifying a substantial reduction in n_{sk}. Fig. 4f shows the contour plots of ρ_{THE} versus T and H and skyrmion phase diagrams after full upward- and downward-poling. In the downward-poling case, the skyrmion phase boundary exhibits a clear shrinkage toward lower H and T, which implies that the thermodynamic stability of skyrmions decreases. As shown in Fig. 4g, the maximum ρ_{THE} decreases almost linearly with the switched FE domain area. In addition, the FE-switching-triggered modifications in THE are highly reproducible (Supplementary Section 8). These results strongly suggest that the FE control of skyrmion properties is truly local, reversible and nonvolatile.

Ferroelectric proximity effect at the atomic scale

Finally, we explore how the FE proximity effect stabilizes and tunes magnetic skyrmions in BTO/STO heterostructures at the atomic scale. Given an ABO_3 perovskite unit cell, FE distortion results in sizeable displacements of the B-site cations with respect to the centre position of the four A-site cations (δ_{A-B}, denoted as δ_{Ba-Ti} and δ_{Sr-Ru} for BTO and SRO, respectively). As our tetragonal BTO film

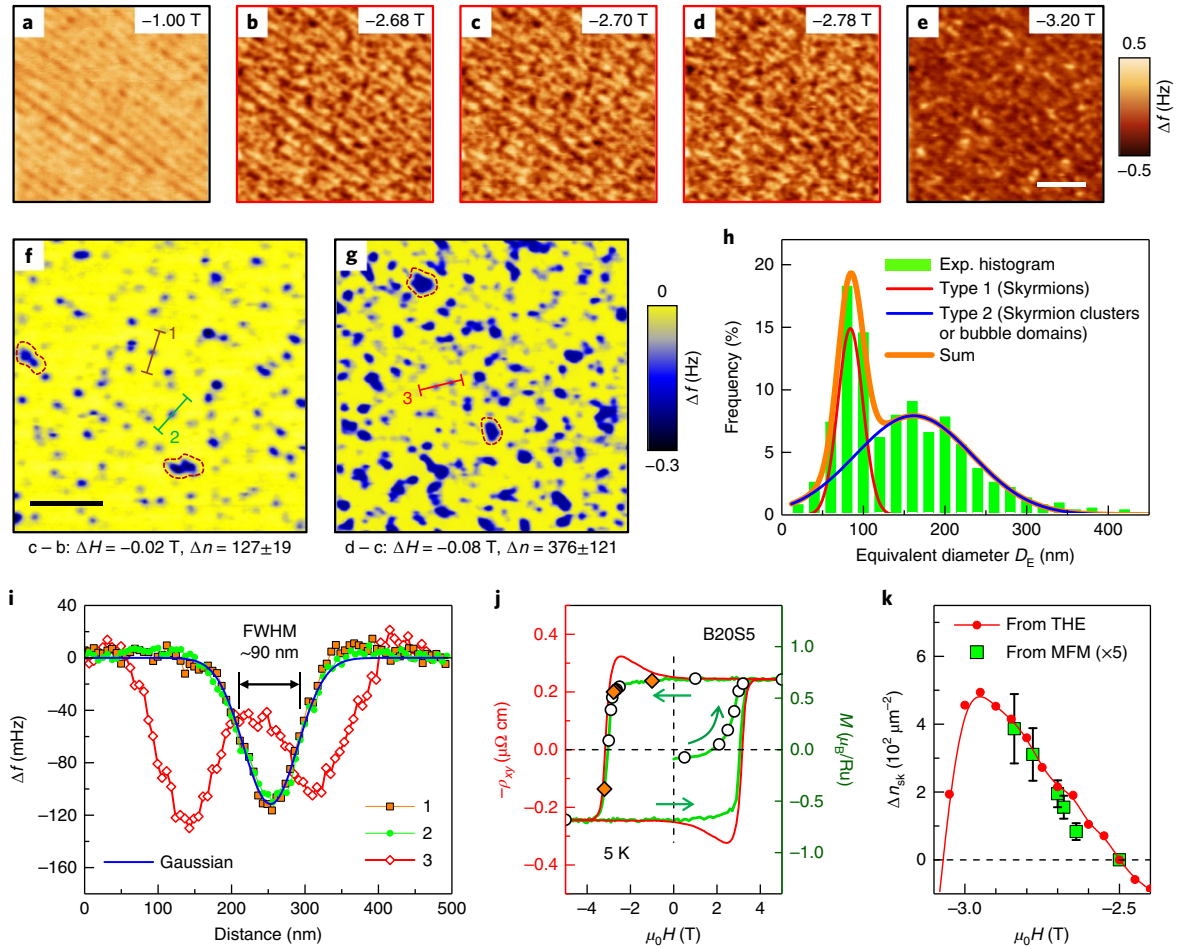

Fig. 3 | Magnetic force microscopy of magnetic skyrmions in the B20S5 sample. a–e, Representative MFM images measured from the B20S5 sample at 5 K at various field strengths as H sweeps from 5 to −5 T. The MFM contrast represents the MFM tip resonant frequency shift (Δf). Negative (positive) Δf signifies the magnetization lies parallel (antiparallel) to the external H. **f**,**g**, MFM images obtained via pixel-by-pixel subtraction on images in **b**, **c** and **d** (framed in red). The number of emergent skyrmions (Δn) and interval of H (ΔH) are labelled. Representative Type 1 and 2 MFM contrasts are marked by solid bars and dotted loops, respectively. The scanning area is 4 × 4 μm. All scale bars correspond to 1 μm. **h**, Statistical histogram of equivalent diameter (D_E), calculated from the area of the domain-like contrast at half-maximum in all the subtracted MFM images. The experimental histogram can be fitted well by two Gaussian distributions. The narrow one peaked at ~90 nm corresponds to Type 1 contrasts (individual skyrmions). The broader one peaked at ~160 nm corresponds to Type 2 contrasts (magnetic bubble domains or skyrmion clusters). **i**, Cross-sectional line profiles of several representative Type 1 MFM contrasts. The full-width-at-half-maximum (FWHM) is ~90 nm. **j**, M–H (green) and ρ_{xy}–H (red) curves measured at 5 K. The H values for taking MFM images are marked by closed rhombi (for images **a**–**e**) and open circles (for the full set of images shown in Supplementary Section 6). **k**, The changes in n_{sk} (Δn_{sk}) derived from ρ_{THE} (solid circles, red) and MFM images (solid squares, green). The error bars represent the upper and lower limits of Δn_{sk}, which were calculated by treating all Type 2 MFM contrasts as skyrmion clusters and individual magnetic bubble domains, respectively.

has [001]-oriented polarization[37], here we consider out-of-plane ionic displacement only. We employed atomically resolved high-angle annular dark-field scanning transmission electron microscopy (HAADF-STEM) to map the δ_{A-B} near the BTO/SRO interfaces. HAADF-STEM images measured from the B20S4 sample along the [100] zone axis with different polarization configurations are shown in Supplementary Section 9. From these images, we calculated and plotted the averaged δ_{A-B} depth profiles in Fig. 5. Positive (negative) δ_{A-B} corresponds to upward (downward) polarization.

The δ_{A-B} depth profiles are highly dependent on the polarization directions. In the upward polarization configuration (top of Fig. 5), the positive δ_{Ba-Ti} are nearly constant and close to the bulk value. Such FE distortion can penetrate into SRO and give rise to a sizeable δ_{Sr-Ru}, which decays gradually within the top three SRO monolayers. The ultrathin SRO film with degraded metallicity may give rise to a rather imperfect carrier screening of FE bound charges. Consequently, the FE-like distortion in SRO becomes energetically favourable in terms of compensating the large depolarization field[32,33]. In the downward polarization configuration (bottom of Fig. 5), by contrast, δ_{Ba-Ti} starts to decrease near the BTO/SRO interface, and δ_{Sr-Ru} also becomes much smaller and confined in the top SRO monolayer only. This structural asymmetry may originate from the extrinsic electron doping in the BTO layer, arising from unavoidable oxygen vacancies. These extra free carriers accumulate near the BTO/SRO interface in the downward polarization configuration. They not only reduce the FE distortion of BTO locally but also provide additional screening of the FE bound charges[32,46]. Therefore, the ionic displacements in both BTO and SRO are suppressed at the interface.

Furthermore, the polarization-dependent δ_{A-B} profile can also explain the high stability and tunability of skyrmion properties. For the upward-poling case, the prominent δ_{Sr-Ru} results in a strong DMI, which decays gradually from the top to bottom SRO monolayers. Such a unique DMI depth profile gives rise to the large

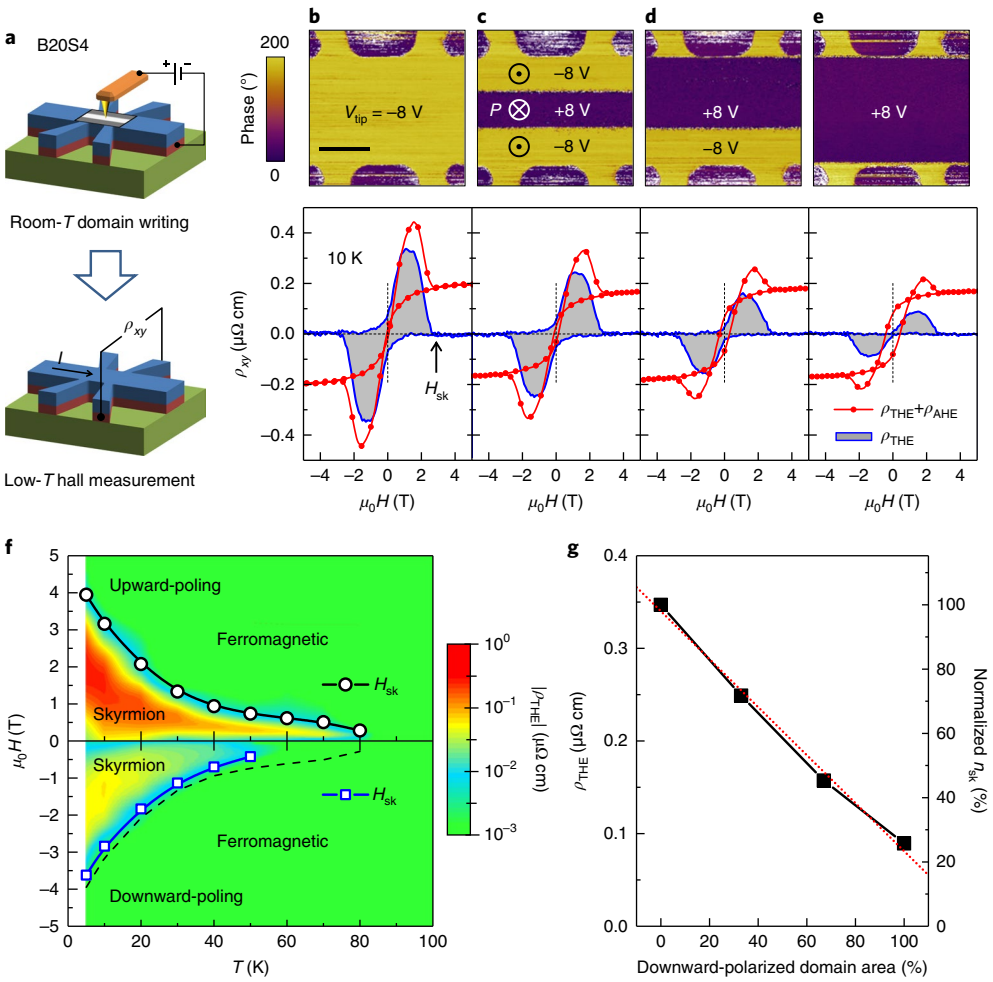

Fig. 4 | FE control of skyrmion properties. a, Schematic diagram of the experimental set-up for FE domain switching and Hall measurements. **b**–**e**, Piezoresponse force microscopy (PFM) phase images (top panels), ρ_{xy}–H and ρ_{THE}–H curves (bottom panels) of the B20S4 sample in different FE poling states. The scale bar in **b** corresponds to 10 μm. The critical H as ρ_{THE} decreases to zero is marked as H_{sk}. **f**, Contour plot of ρ_{THE} and the skyrmion phase diagrams measured in the fully upward- and downward-poling configurations. Only one THE branch is shown in either plot for clarity. The H_{sk}–T curves represent the phase boundaries between the skyrmion and ferromagnetic phases. In the bottom panel, the H_{sk}–T curve in the upward-poling case is also inserted as a dashed line for comparison. Clearly, the phase boundary shrinks toward lower H and T for the downward-poling case. **g**, The maximum ρ_{THE} and corresponding normalized n_{sk} as a function of the downward-polarized domain area. As highlighted by the dashed guideline (red), the change in ρ_{THE} follows an almost linear trend.

n_{sk} and high stability of skyrmions (see Supplementary Sections 9 and 10 for detailed analyses). In contrast, for the downward-poling case, the δ_{Sr-Ru} is much weaker. Consequently, D_{eff} decreases substantially, inevitably reducing both n_{sk} and the thermodynamic stability. Notably, reversal of the DMI vector should not change the sign of ρ_{THE} (Supplementary Note 2), which is consistent with our observations in Fig. 4b–e. We further characterized the OHE, AHE and longitudinal transport properties of the BTO/SRO samples for different polarization configurations (Supplementary Section 8). These results confirmed that the FE-modulations of carrier density and magnetism are minor and have negligible effects on the skyrmion properties[47]. The FE control of skyrmion properties should be dominated by the direct modulations of the DMI.

Summary and outlook

We exploited the ultrathin BTO/SRO heterostructure as a platform hosting small and highly tunable magnetic skyrmions. In this system, the FE proximity effect near the BTO/SRO interface gives rise to an emergent DMI, thereby creating robust magnetic skyrmions. By harnessing the FE polarization of the BTO capping layer, we achieved local, switchable and nonvolatile control of the density and stability of magnetic skyrmions.

The ferroelectrically tunable magnetic skyrmions in BTO/SRO heterostructures allow remarkable versatility when designing and fabricating skyrmion-based devices. Domain switching in FE thin films can be achieved at various length scales, ranging from micrometres to nanometres[44,45,48]. By downscaling the FE domain size, it is possible to not only tune the overall skyrmion properties microscopically (as demonstrated herein) but also realize the nucleation/deletion of individual skyrmions. Moreover, such a multi-scale tunability can be achieved in skyrmions with typical diameters below 100 nm, which could be potentially suitable for both electrical detection and high-density integration[2]. On this basis, FE/ferromagnetic ultrathin oxide heterostructures could offer an effective approach to simultaneously improve the integration and addressability of skyrmion-based devices. Furthermore, this all-oxide skyrmion system can be flexibly and epitaxially grown with other functional oxide heterostructures. This compelling advantage offers a fertile playground for exploring emergent phenomena that arise from interfacing magnetic skyrmions with additional functionalities[31].

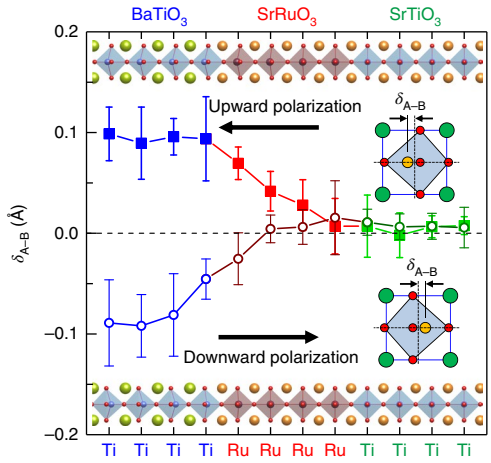

Fig. 5 | Scanning transmission electron microscopy results near the BTO/SRO interface. Ionic displacement (δ_{A-B}) profiles derived from the atomically resolved HAADF-STEM images of the B20S4 sample (included in Supplementary Section 9). In each perovskite unit cell, δ_{A-B} is calculated from the displacement along the [001] axis between the B-site cation and the centre position of four A-site cations. The δ_{A-B} values are averaged over each perovskite monolayer, and the error bars represent the standard deviations. Positive (negative) δ_{A-B} corresponds to the upward (downward) polarization configuration, which is plotted in solid squares (open circles). The schematics of ionic displacement patterns and unit-cell structures in both polarization configurations are shown in the insets.

Online content

Any methods, additional references, Nature Research reporting summaries, source data, statements of data availability and associated accession codes are available at https://doi.org/10.1038/s41563-018-0204-4.

Received: 9 April 2018; Accepted: 21 September 2018;
Published online: 05 November 2018

References

1. Nagaosa, N. & Tokura, Y. Topological properties and dynamics of magnetic skyrmions. *Nat. Nanotech.* **8**, 899–911 (2013).
2. Fert, A., Reyren, N. & Cros, V. Magnetic skyrmions: advances in physics and potential applications. *Nat. Rev. Mater.* **2**, 17031 (2017).
3. Mühlbauer, S. et al. Skyrmion lattice in a chiral magnet. *Science* **323**, 915–919 (2009).
4. Sampaio, J., Cros, V., Rohart, S., Thiaville, A. & Fert, A. Nucleation, stability and current-induced motion of isolated magnetic skyrmions in nanostructures. *Nat. Nanotech.* **8**, 839–844 (2013).
5. Hagemeister, J., Romming, N., Von Bergmann, K., Vedmedenko, E. Y. & Wiesendanger, R. Stability of single skyrmionic bits. *Nat. Commun.* **6**, 8455 (2015).
6. Yu, X. Z. et al. Real-space observation of a two-dimensional skyrmion crystal. *Nature* **465**, 901–904 (2010).
7. Heinze, S. et al. Spontaneous atomic-scale magnetic skyrmion lattice in two dimensions. *Nat. Phys.* **7**, 713–718 (2011).
8. Milde, P. et al. Unwinding of a skyrmion lattice by magnetic monopoles. *Science* **340**, 1076–1081 (2013).
9. Jiang, W. et al. Blowing magnetic skyrmion bubbles. *Science* **349**, 283–286 (2015).
10. Woo, S. et al. Observation of room-temperature magnetic skyrmions and their current-driven dynamics in ultrathin metallic ferromagnets. *Nat. Mater.* **15**, 501–506 (2016).
11. Büttner, F. et al. Field-free deterministic ultrafast creation of magnetic skyrmions by spin–orbit torques. *Nat. Nanotech.* **12**, 1040–1044 (2017).
12. Romming, N. et al. Writing and deleting single magnetic skyrmions. *Science* **341**, 636–639 (2013).
13. Fert, A., Cros, V. & Sampaio, J. Skyrmions on the track. *Nat. Nanotech.* **8**, 152–156 (2013).
14. Röβler, U. K., Bogdanov, A. N. & Pfleiderer, C. Spontaneous skyrmion ground states in magnetic metals. *Nature* **442**, 797–801 (2006).
15. Dzyaloshinsky, I. A thermodynamic theory of 'weak' ferromagnetism of antiferromagnetics. *J. Phys. Chem. Solids.* **4**, 241–255 (1958).
16. Moriya, T. Anisotropic superexchange interaction and weak ferromagnetism. *Phys. Rev.* **120**, 91–98 (1960).
17. Siemens, A., Zhang, Y., Hagemeister, J., Vedmedenko, E. Y. & Wiesendanger, R. Minimal radius of magnetic skyrmions: statics and dynamics. *New J. Phys.* **18**, 045021 (2016).
18. Seki, S. et al. Observation of skyrmions in a multiferroic material. *Science* **336**, 198–201 (2012).
19. Kezsmarki, I. et al. Néel-type skyrmion lattice with confined orientation in the polar magnetic semiconductor GaV_4S_8. *Nat. Mater.* **14**, 1116–1122 (2015).
20. Moreau-Luchaire, C. et al. Additive interfacial chiral interaction in multilayers for stabilization of small individual skyrmions at room temperature. *Nat. Nanotech.* **11**, 444–448 (2016).
21. Soumyanarayanan, A. et al. Tunable room temperature magnetic skyrmions in Ir/Fe/Co/Pt multilayers. *Nat. Mater.* **16**, 898–904 (2017).
22. Schott, M. et al. The skyrmion switch: Turning magnetic skyrmion bubbles on and off with an electric field. *Nano. Lett.* **17**, 3006–3012 (2017).
23. Maccariello, D. et al. Electrical detection of single magnetic skyrmion at room temperature. *Nat. Nanotech.* **13**, 233–237 (2018).
24. Ohuchi, Y. et al. Electric-field control of anomalous and topological Hall effects in oxide bilayer thin films. *Nat. Commun.* **9**, 213 (2018).
25. Hsu, P. J. et al. Electric-field-driven switching of individual magnetic skyrmions. *Nat. Nanotech.* **12**, 123–126 (2017).
26. Cheong, S. W. & Mostovoy, M. Multiferroics: A magnetic twist for ferroelectricity. *Nat. Mater.* **6**, 13–20 (2007).
27. Ruff, E. et al. Multiferroicity and skyrmions carrying electric polarization in GaV_4S_8. *Sci. Adv.* **1**, e1500916 (2015).
28. Chakraverty, S. et al. Multiple helimagnetic phases and topological Hall effect in epitaxial thin films of pristine and Co-doped $SrFeO_3$. *Phys. Rev. B* **88**, 220405(R) (2013).
29. Ahadi, K., Galletti, L. & Stemmer, S. Evidence of a topological Hall effect in $Eu_{1-x}Sm_xTiO_3$. *Appl. Phys. Lett.* **111**, 172403 (2017).
30. Matsuno, J. et al. Interface-driven topological Hall effect in $SrRuO_3$–$SrIrO_3$ bilayer. *Sci. Adv.* **2**, e1600304 (2016).
31. Hwang, H. Y. et al. Emergent phenomena at oxide interfaces. *Nat. Mater.* **11**, 103–113 (2012).
32. Gerra, G., Tagantsev, A. K., Setter, N. & Parlinski, K. Ionic polarizability of conductive metal oxides and critical thickness for ferroelectricity in $BaTiO_3$. *Phys. Rev. Lett.* **96**, 107603 (2006).
33. Chisholm, M. F., Luo, W., Oxley, M. P., Pantelides, S. T. & Lee, H. N. Atomic-scale compensation phenomena at polar interfaces. *Phys. Rev. Lett.* **105**, 197602 (2010).
34. Shin, Y. J. et al. Interface control of ferroelectricity in an $SrRuO_3/BaTiO_3/SrRuO_3$ capacitor and its critical thickness. *Adv. Mater.* **29**, 1602795 (2017).
35. Guo, H. et al. Interface-induced multiferroism by design in complex oxide superlattices. *Proc. Natl Acad. Sci.* **114**, E5062–E5069 (2017).
36. Mattheiss, L. F. Electronic structure of RuO_2, OsO_2, and IrO_2. *Phys. Rev. B* **13**, 2433–2450 (1976).
37. Kwei, G. H., Lawson, A. C., Billinge, S. J. L. & Cheong, S. W. Structures of the ferroelectric phases of barium titanate. *J. Phys. Chem.* **97**, 2368–2377 (1993).
38. Wang, L. et al. Electronic-reconstruction-enhanced-tunneling conductance at terrace edges of ultrathin oxide films. *Adv. Mater.* **29**, 1702001 (2017).
39. Koster, G. et al. Structure, physical properties, and applications of $SrRuO_3$ thin films. *Rev. Mod. Phys.* **84**, 253–298 (2012).
40. Yu, X., Tokunaga, Y., Taguchi, Y. & Tokura, Y. Variation of topology in magnetic bubbles in a colossal magnetoresistive manganite. *Adv. Mater.* **29**, 1603958 (2017).
41. Pollard, S. D. et al. Observation of stable Néel skyrmions in cobalt/palladium multilayers with Lorentz transmission electron microscopy. *Nat. Commun.* **8**, 14761 (2017).
42. Yagil, A. et al. Stray field signatures of Néel textured skyrmions in Ir/Fe/Co/Pt multilayer films. *Appl. Phys. Lett.* **112**, 192403 (2018).
43. Nakazawa, K., Bibes, M. & Kohno, H. Topological Hall effect from strong to weak coupling. *J. Phys. Soc. Japan* **87**, 033705 (2018).
44. Ahn, C. H., Rabe, K. M. & Triscone, J.-M. Ferroelectricity at the nanoscale: local polarization in oxide thin films and heterostructures. *Science* **303**, 488–491 (2004).
45. Cen, C. et al. Nanoscale control of an interfacial metal–insulator transition at room temperature. *Nat. Mater.* **7**, 298–302 (2008).
46. Liu, X., Tsymbal, E. Y. & Rabe, K. M. Polarization-controlled modulation doping of a ferroelectric from first principles. *Phys. Rev. B* **97**, 094107 (2018).
47. Ahn, C. H. et al. Electrostatic modification of novel materials. *Rev. Mod. Phys.* **78**, 1185–1212 (2006).
48. Dawber, M., Rabe, K. M. & Scott, J. F. Physics of thin-film ferroelectric oxides. *Rev. Mod. Phys.* **77**, 1083–1130 (2005).

Acknowledgements

Q.L., W.M. and Q.F. were supported by the National Key R&D Program of China (grants no. 2017YFA0402903 and no. 2016YFA0401003) and the National Natural Science Foundation of China (grant no. 51627901). J.H.H. was supported by Samsung Science and Technology Foundation under Project Number SSTF-BA1701-07. STEM and PPMS measurements were supported by the National Center for Inter-University Research Facilities (NCIRF) at Seoul National University in Korea. All the authors want to acknowledge major support from the Research Center Program of IBS (Institute for Basic Science) in Korea (IBS-R009-D1). We also acknowledge invaluable suggestions and support from S.Y. Park, S.M. Yang, S. H. Chang, C. Kim, J.-G. Park, B.J. Yang, T.H. Kim, W. Wu and Y. Wang.

Author contributions

L.W. and T.W.N. conceived the idea and designed the experiments. R.K. performed the first-principles DFT calculations. L.W. and Y.J.S. grew the samples, fabricated the Hall bar devices and performed the PFM measurements. Y.K. and M.Y.K. performed the STEM measurements. Q.F., H.Z., W.M. and Q.L. performed the MFM measurements. S.D.P., K.H.L. and H.Y. performed the numerical simulations on skyrmion stability. L.W. and T.W.N. analysed the results and wrote the manuscript. All authors participated in the discussions during manuscript preparation.

Competing interests

The authors declare no competing interests.

Additional information

Supplementary information is available for this paper at https://doi.org/10.1038/s41563-018-0204-4.

Reprints and permissions information is available at www.nature.com/reprints.

Correspondence and requests for materials should be addressed to L.W. or Q.L. or T.W.N.

Publisher's note: Springer Nature remains neutral with regard to jurisdictional claims in published maps and institutional affiliations.

Methods

DFT calculations. DFT calculations were performed using the Vienna ab initio simulation (VASP) code[49]. The supercell used to calculate the DMI (exchange interaction) was constructed from a $4\times3\times3$ ($\sqrt{2}\times\sqrt{2}\times2$) SRO pseudo-cubic unit cell. We manually imposed the ionic displacement δ_{Ru-O} in the [001] direction to artificially create FE-like distortion in the SRO lattice. We varied the magnitude of δ_{Ru-O} from 0 to 0.25 Å. The DMI constant D and exchange stiffness J were determined by mapping the total energies of artificially imposed spin configurations on the Hamiltonian $H=-J\sum_{ij}\mathbf{S}_i\cdot\mathbf{S}_j+D\sum_{ij}\mathbf{d}_{ij}\cdot(\mathbf{S}_i\times\mathbf{S}_j)$ (refs [50,51]). The details are described in Supplementary Section 1. Only the DMI and exchange coupling between nearest-neighbouring spins in the xy plane were considered in the calculations. The projector-augmented-wave method and the exchange-correlation functional of the generalized gradient approximation in the Perdew–Burke–Ernzerhof scheme were employed[52]. All the relativistic effects, including spin–orbit coupling were included. The cutoff energy for the plane-wave basis set was 500 eV. Approximately 10,000 k-points per reciprocal atom were used for all calculations.

Film growth and structural characterizations. SRO and BTO films were fabricated using a pulsed-laser deposition system with a KrF excimer laser. Prior to deposition, STO(001) substrates with low-miscut-angles (0.05~0.1°) were etched using buffered hydrofluoric acid and annealed in the ambient atmosphere, to create atomically smooth TiO_2-terminated surfaces with one-unit-cell-high terrace structure. During deposition, the temperature of the substrate was maintained at 700 °C. The SRO ultrathin films were grown under an oxygen pressure of 100 mtorr with a laser fluence of 2 J cm^{-2}. The BTO layers were subsequently deposited at an oxygen pressure of 5 mtorr with a laser fluence of 1 J cm^{-2}. The time-dependent intensity of the reflection high-energy electron diffraction patterns (Supplementary Section 2) indicates that SRO films grew in a step-flow mode, whereas the BTO films grew in a two-dimensional (2D) layer-by-layer mode.

HAADF-STEM measurements and analysis. All the HAADF-STEM images were measured using a Cs-corrected STEM (JEM-ARM200F; JEOL). Atomic positions were determined by simultaneously fitting all atomic peaks using 2D Gaussian functions via a Matlab code. The displacements of B-site cations with respect to the centres of four A-site cations were calculated in each perovskite unit cell. We defined the out-of-plane component of the ionic displacement as δ_{A-B} and neglected the in-plane component due to the very tiny magnitude.

PFM measurements. PFM measurements were performed at room temperature using a commercial scanning probe microscope (Cypher, MFP-3D; Asylum Research) and Ir/Pt-coated AFM tips (PPP-EFM; Nanosensors). The PFM hysteresis loops and images were collected from the BTO films in the dual alternating current resonance tracing (DART) mode. The typical tip radius was −10 nm, and the force constant was ~3 N m^{-1}. Before the PFM imaging or low-temperature Hall measurements, BTO films were electrically poled into pre-designed domain structures using a conducting AFM tip ($V_{tip}=\pm8$ V). To ensure homogenous domain switching, the fast scan velocity of the biased tip was set below 10 μm s^{-1}.

Low-temperature magnetism and transport measurements. M–T and M–H curves were recorded using a SQUID magnetometer (MPMS; Quantum Design) with H applied along the out-of-plane direction. The longitudinal and transverse transport data were measured using a physical properties measurement system (PPMS, Quantum Design) on standard Hall bars. Conventional photolithography and ion-milling were used to pattern the BTO/SRO films into the Hall bar geometry. The channel size was minimized to 20×20 μm^2. After patterning, the samples were ex-situ annealed at 600 °C in ambient oxygen flow for 1 h to minimize the oxygen deficiency induced during growth and ion-milling. Ti (5 nm) and Pt (50 nm) films were sputtered onto the Hall bar as contact electrodes. After the entire fabrication process, the BTO/SRO conducting channels still exhibit atomically-flat topography and robust ferroelectricity (Supplementary Section 7). The Hall bars were electrically connected to a custom-built chip adaptor to enable quick transfer (within 20 min) from the PFM measurement set-up to the PPMS.

MFM experiments. MFM experiments were performed using a custom-designed variable temperature MFM system, equipped with a 20 T superconducting magnet[53]. We incorporate a commercial piezoresistive cantilever (PRC400; Hitachi High-Tech Science Corporation) as the force sensor. The resonant frequency of the cantilever is about 42 kHz. The MFM tip has a magnetic coating consisting of 5 nm Cr, 50 nm Fe and 5 nm Au films. This magnetic coating was magnetized perpendicular to the cantilever. The H_C and saturation fields are ~250 Oe and ~2,000 Oe, respectively. A built-in phase-locked loop (R9 controller; RHK Technology) was used for MFM scanning control and signal processing. During the MFM imaging, we first measured the topographic image using a contact mode and compensated the sample surface tilting along the fast and slow scan axes. Then we lifted the tip by ~100 nm to the surface and measured the MFM images in a frequency-modulation mode. The experiment details can be found in Supplementary Section 6.

Data availability

All relevant data that support the plots within this paper are available from the corresponding author upon reasonable request.

References

49. Kresse, G. & Furthmüller, J. Efficient iterative schemes for *ab initio* total-energy calculations using a plane-wave basis set. *Phys. Rev. B* **54**, 11169–11186 (1996).
50. Xiang, H. J., Kan, E. J., Wei, S. H., Whangbo, M.-H. & Gong, X. G. Predicting the spin-lattice order of frustrated systems from first principles. *Phys. Rev. B* **84**, 224429 (2011).
51. Yang, H., Thiaville, A., Rohart, S., Fert, A. & Chshiev, M. Anatomy of Dzyaloshinskii–Moriya interaction at Co/Pt interfaces. *Phys. Rev. Lett.* **115**, 267210 (2015).
52. Perdew, J. P., Burke, K. & Ernzerhof, M. Generalized gradient approximation made simple. *Phys. Rev. Lett.* **77**, 3865–3868 (1996).
53. Zhou, H. et al. Evolution and control of the phase competition morphology in a manganite film. *Nat. Commun.* **6**, 8980 (2015).